CHAPTER 1

PRECISION LUMINOSITY MEASUREMENT

1.0.1 Introduction

The CEPC machine detector interface (MDI) region is optimized with a 20 mm diameter beam-pipe at the Interaction Point (IP), which splits into dual pipes for the 33 mRad beam crossing of electron and positron beams. The MDI instrumentation is illustrated in Fig. 1.1. The luminometer is positioned within the inner beam-pipe within the flanges at $|z| = 700$ mm and before the quadrupole magnets in the low angle region of less than 100 mRad to the laboratory (LAB) frame. The e^+e^- collision luminosity is measured by counting Bhabha elastic scattering in the Luminosity Calorimeter (LumiCal) with silicon position detectors and rad-hard LYSO crystals with the precision depending on the acceptance fiducial edges.

The CEPC instant luminosity is designed for $8.3 \times 10^{34}/cm^2s$ and $1.9 \times 10^{36}/cm^2s$ at the HZ and Z-pole operation modes (50MW plan), at center of mass energies of $\sqrt{s} = 240$ and 91 GeV, respectively. The yield with two IPs will be 4 million HZ and 4 trillion Z boson events. With such a high event statistics, the measurement on Standard Model processes requires the precision on luminosity of better than 10^{-4} at the Z-pole.

Bhabha events are detected with a pair of electron and position back-to-back in direction, each with momentum of the beam energy. The LumiCal design has to incorporate the limited space in the forward region with the minimum upstream materials to reduce multiple scattering of the electron tracking precision, and sufficient radiation length for LYSO crystal calorimeter, and maximum phase space coverage for the Bhabha event acceptance. The LumiCal design within the beam-pipe flanges (Fig. 1.1.b) includes two layers of Si-wafers in front of 2 X_0 LYSO crystals in each sides of the flanges. Behind the flanges and bellows of a total 4.3 X_0 of steel (Fig. 1.1.c), mounted on the quadrupole magnets are 17.4 X_0 of LYSO calorimeter for detection of electrons.

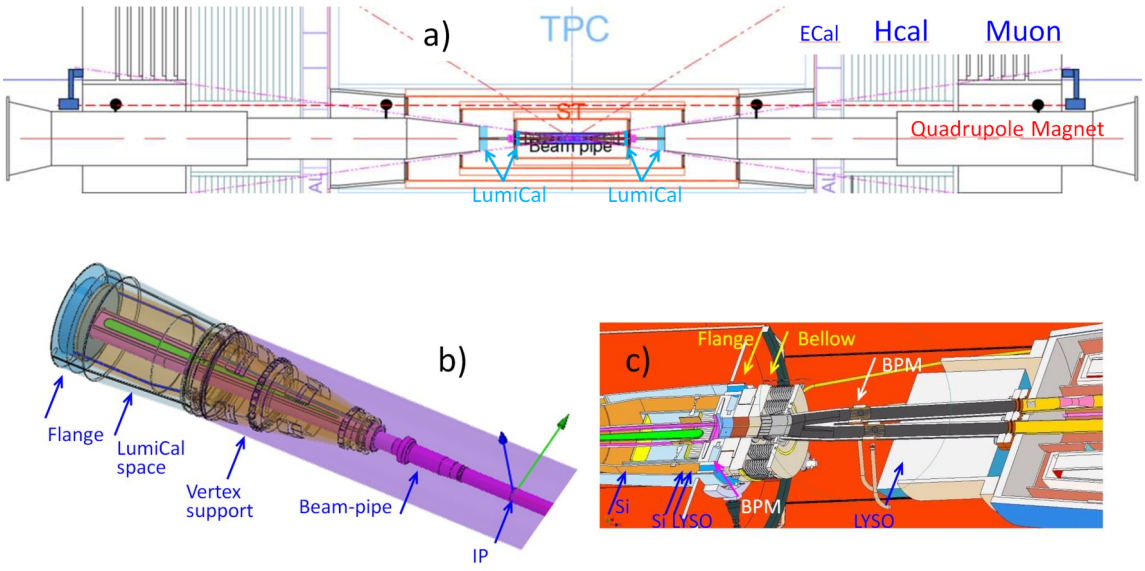

Figure 1.1 The MDI region is illustrated in a) the yz-view across the two quadrupole magnets; b) the IP to beam-pipe flange at $|z| = 700$ mm showing the beam-pipe (purple) vertex detector support and the volume before flange (blue) for LumiCal; c) the x-z cut view of the LumiCal before flange, the bellow, and the long crystal before the BPMs and the quadrupole magnet.

The QED calculation for Bhabha interaction is precise to next-to-leading order (NLO) of $e^+e^- \to e^+e^-\gamma$. The BHLUMI event generator [1] developed at LEP for low-angle Bhabha cross section has being precise to 0.037% [2]. A recent developed event generator, ReneSANCe [3] has reported consistency with BHLUMI and potential deviation at the 0.01% level with electrons scattered with high θ angles. The higher order corrections to Bhabha interaction are being motivated for future e^+e^- collider projects toward 0.01% precision.

The leading order of Bhabha cross section, integrated over an angular coverage of ($\theta_{min} < \theta < \theta_{max}$), is

$$\sigma = \frac{16\pi\alpha^2}{s}\left(\frac{1}{\theta^2_{min}} - \frac{1}{\theta^2_{max}}\right). \tag{1.1}$$

The integrated luminosity ($\mathcal{L}$) with N_{acc} Bhabha events detected is,

$$\mathcal{L} = \frac{1}{\epsilon}\frac{N_{acc}}{\sigma}, \qquad \frac{\Delta\mathcal{L}}{\mathcal{L}} \sim \frac{2\Delta\theta}{\theta_{min}}. \tag{1.2}$$

where ϵ is the detection efficiency to be evaluated. The systematic uncertainties are attributed mostly by the error on θ_{min}, mainly due to mechanical alignment and detector resolution. The error propagates to the luminosity is twice higher. Assuming the θ_{min} threshold for Bhabha detected is set to 20 mRad, the deviation $\Delta\theta$ corresponding to 10^{-4} error in luminosity is 1 μRad. At a distance of $|z| = 1$ m from the IP, the tolerance is 1μm.

The location of luminometer is favorable for lower θ_{min} to increase Bhabha cross section that has a $1/\theta^2$ dependence. The front LumiCal Si-wafer is located at $|s| = 560$ mm. The race-track beam pipe has an inner radius of 10 mm. Assuming the detector acceptance edge is 12 mm from the beam pipe center, the corresponding θ_{min} is 21.4 mRad.

Illustrated in Fig. 1.2.a is the drawing of MDI volume before the flange, and in Fig. 1.2.b the LumiCal including the LYSO crystals between the bellow and BPM. The latest design of quadrupole magnet has the front front surface located at $|z| = 1050$ mm, and the LYSO bars at $|z| = 800$ to 950 mm.

The x-y projection of LumiCal is plotted in Fig. 1.3.a, with the trace-track beam-pipe expanding from the IP of a 10 mm diameter Be tube to dual, 3 mm thick copper pipes. The LumiCal modules are separated above and below the beam pipe, the dimension of components before the flange are illustrated in Fig. 1.3.b for the second layer of Si-wafer and the 2 X_0 LYSO bars.

The beam-crossing results to boost of electrons in +x axis toward the outgoing beam-pipe direction. The detector modules are spared between $|y| > 12$ mm off the beam-pipe height, as in this region the Bhabha electron on the -x side is lost into the beam-pipe. A meaningful back-to-back electron pairs can not be selected.

Surrounding the out-going pipe, the Bhabha electron rate is the highest. The fast luminosity monitor detecting single Bhabha electrons has a ideal position at the +x side of beam-pipe near the quadrupole, where the θ angle corresponds to around 10 mRad, that has the highest event rate physics (QED Bhabha and SM) interactions. The fast luminosity monitor using Diamond detector can endure radiation for detection of e^+e^- collisions to provide on-line luminosity measurement. The location of fast luminosity monitor is illustrated in Fig. 1.3.c.

We discuss the technical design of luminometer in the following sections. In Section 1.0.2 the fast luminosity monitor at the lowest angle before the quadru-pole magnet is discussed. The electron shower distribution of a electron traversing 3 mm copper pipe is simulated with the GEANT program. The detector option is considered for a fine pitch diamond strip detector that can endure the strong radiation field. The prototyping of diamond detector for strip implantation, and the response to ionization of a MIP particle are discussed.

The beam steering will rely on the Beam Position Monitors (BPMs) implemented inside the beam-pipe flanges and before the quadrupole magnets. The functionalities and precision for measuring beam currents and the crossing at IP are discussed in Section 1.0.3. The colliding electron and position bunches will be monitored for the beam currents in $x - y$ directions and timing indicting the z position, to identify deviation of the IP.

The Bhabha acceptance in the MDI volume is investigate with the BHLUMI which is discussed in Section 1.0.4, for the LumiCal coverage corresponding to $\theta > 25$ mRad, $|y| > 25$ mm at $|z| = 1000$ mm. With both scattered electrons of Bhabha events detected, the cross section at Z-pole is estimated to be 78 nb. It is about twice of the $Z \to q\bar{q}$ channel (41 nb) for Z line-shape study.

To advance measurement for radiative Bhabha measurement, in Section 1.0.5 we compare NLO QED generators and detection of the final state ISR or FSR photons. The BHLUMI generator is developed based on the Yennie-Frautschi-Suura (YFS) exponentiation algorithm [4, 5] to sum up contribution of real and virtual radiation photons, with cancellation of infrared divergent terms to all orders in α. Bhabha calculation based on Feynman diagrams are approaching 0.01% precision. The ReneSANCe calculate NLO diagram adding one final state photons. The two generators show different amount of photons generated. Measurement of radiative Bhabha with initial or final state radiations shall be conducted to confirm the theoretical NLO description.

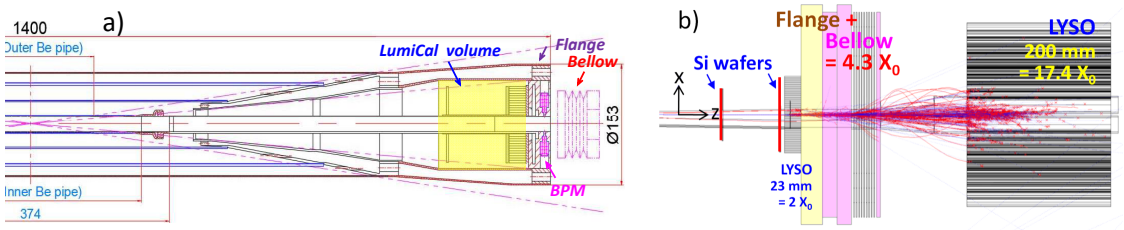

Figure 1.2 The LumiCal volume before the flange is shown in a), where two Si-wafers are positioned before 2 X_0 LYSO bars. Inside the flanges in each side, four Beam Position Monitors are installed. b) the LumiCal is shown with a 50 GeV electron shower illustrated. Before the flange, the Si-wafers with short LYSO crystals provide electron θ position with e/γ veto. The long LYSO behind the bellow provide beam electron identification by energy deposits. The LYSO length has assumed for 200 mm.

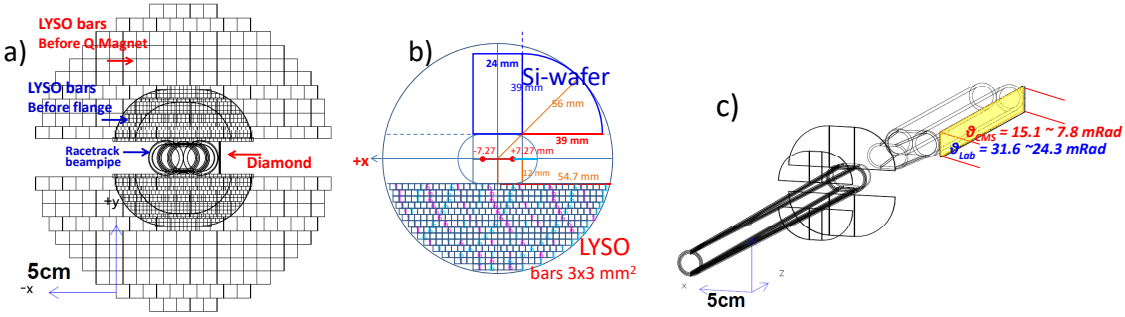

Figure 1.3 The projection of LumiCal design is illustrated in a), with the racetrack beam pipe from IP to quadrupole. The design of the second Si-wafer at $|z| = 640$ mm and the 2 X_0 of LYSO bars mounted on the flanges are plotted in b). The front LYSO bars dimension is $3 \times 3 \times 23$ mm^3. The long LYSO modules behind the bellow are segmented in $10 \times 10 \times 200$ mm^3. The fast monitoring diamond detectors in c) are positioned between the long LYSO modules on the sides of electron boosted direction, where the Bhabha electron rate is the highest.

The LumiCal design has been revised continuously with the beam pipe design, from the original 30 mm round pipe, to the latest race-track design with $\phi = 20$ mm at IP. The earliest detector technology has assumed a Si-W sandwiched assembly, which is reported in CDR. To accommodate the limited space in the forward MDI region, the latest assembly with Si-wafers and LYSO crystals is discussed in Section 1.0.6.

The LYSO crystal has better radiation tolerance that can be equipped with SiPM read-out for compactness of front-end electronics. The LYSO modules of the LumiCal are discussed in Section 1.0.7, for the finely segmented $2X_0$ bars positioned before beam-pipe flanges, and the long $17.3X0$ in space before the quadrupole magnets. The front LYSO bars with Si-wafers will distinguish e, γ for detection of radiative Bhabha events. The simulation of electron showers in LYSO are discussed.

The systematics are discussed in Section 1.0.8 for deviations sensitive to the LumiCal fiducial acceptance of low-theta edges. The 10^{-4} precision corresponds to 1 μRad at $\theta = 20$ mRad. The uncertainties are itemized for the beam-dynamics on E_b and energy spread, beam-current measurement by BPMs and off-set at IP, LumiCal Si-wafer position deviation, and monitoring of the beam-pipe position. The detector assembly can have

the Si-wafer positions well surveyed to sub-micron level. However, once installed on the MDI, the position monitoring shall be instrumented with the error on means better than 1 μRad, which which corresponds to the offset of flanges smaller than 0.7 μm in x-y and 35 μm in z direction.

A summary in Section 1.0.9 discuss the the integrated luminosity that will be corrected for the IP and detector positions monitored with the error on means of less than 1 μRad.

1.0.2 Fast Luminosity Monitor

The fast luminosity monitor is consider for instant feedback of beam collisions for steering of beam position with external detectors. We propose for detecting scattering of small angle Bhabha electrons in the detector volume. The location is by the beam pipe before the quadrupole magnet, where the polar angle corresponds to $\theta \sim 10$ mRad. This corner has the highest e^+e^- collisions events, in part due to the beam-cross of 33 mRad to boost small angle Bhabha electrons out of beam pipe.

Illustrated in Fig. 1.4.a is a shower event of a 50 GeV electron traversing the 3 mm copper beam pipe at 10 mRad. In Fig. 1.4.b the Bhabha electrons of BHLUMI are plotted surrounding the beam-pipe between $|z| = 855$ to 1110 mm, where the LYSO crystals are located before the quadrupole magnet. The blue bar indicate the location of fast luminosity monitor. At this position, the radiation field is the highest at CEPC. The most radiation tolerant detector to be considered is a diamond slab segmented in strips to detect electron showers generated in the copper beam pipe.

The electron shower profiles generated in the 3 mm copper beam pipe is investigated with GEANT, with tubes positioned parallel to z-axis at center $|x| = 13mm$ and 0.4 mm thick diamond slab at $x = -27$ mm, with the height of $y = \pm 12$ and length $|z| = 855$ to 1110 mm. Electrons were generated at around 10 mRad at $y = 0$ to the diamond. The beam-crossing of 33 mRad corresponds to boost of 16.5 mRad to the electrons. Fig. 1.5.a show the y-z contours of 50 GeV electron showers are theta angles from 9 to 12 mRad, showing a offsets of wide distributions with RMS of 30 mm (Fig. 1.5.b). The shower profiles are compared for offsets of the IP, that may help beam steering. The deviation on x position can be sensitive to 0.1 mm level, and z position deviation of around 10 mm.

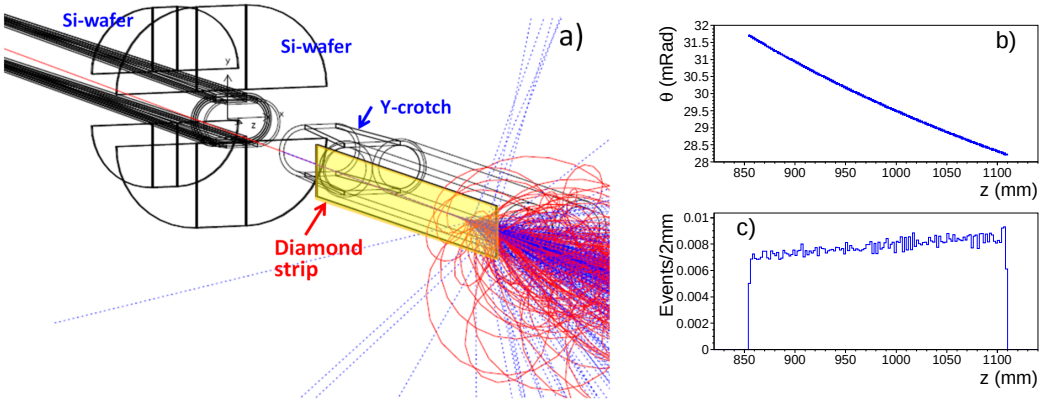

Figure 1.4 A shower passing 3 mm Cu beam-pipe is shown in a), for a 50 GeV electron at 10 mRad to the outgoing beam direction of 16.5 mRad. The diamond slab (24×320 mm^2) is located on the side of beam-pipe at 13 mm to beam center. The hits on diamond slab is ploted in b) for the theta versus z in laboratory frame. The event rate (normalized to 1) in z is plotted in c).

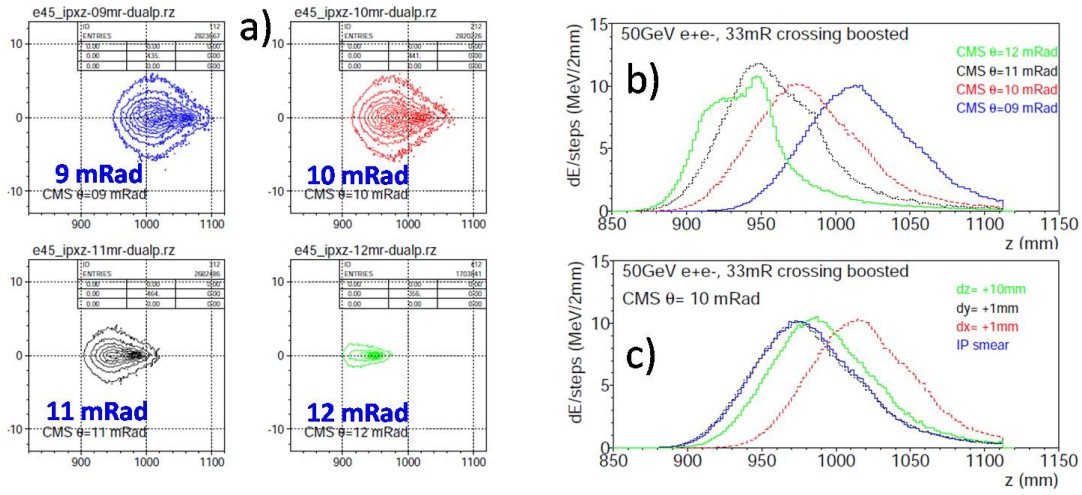

Figure 1.5 Electron shower profiles are shown a) the y-z counters with CMS θ from 9 to 12 mRad, being boosted ($+16.5$ mRad), at $y = 0$/ The dE/dx deposition in z is shown in b). The sensitivity to IP offsets are plotted in c).

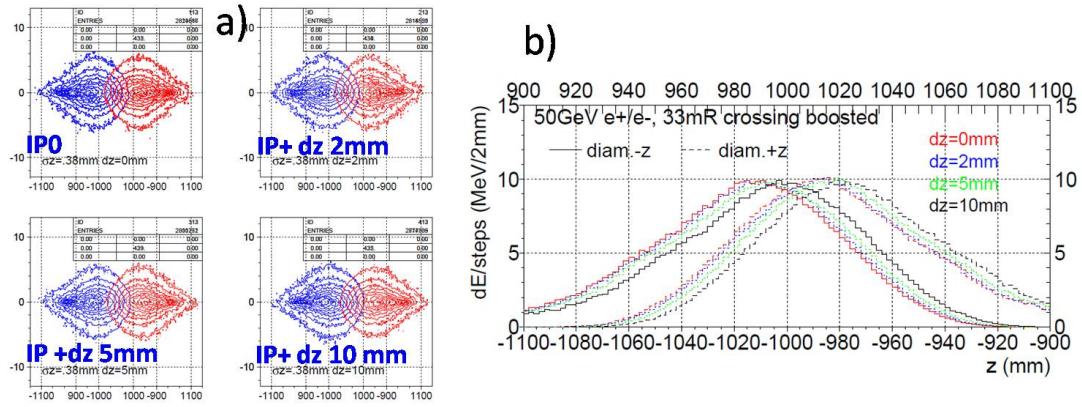

Figure 1.6 a) the contours of y-z shower profiles of both z-sides are shown for various dz offsets of IP; the corresponding dE/dx profiles in z plotted in b).

The fast luminosity monitors assist beam steering by observing scattering of electrons on both z-sides. The electrons shower profiles are observed event by event. The integrated events rates along the z-positions can help monitoring the z-position of IP. Illustrated in Fig. 1.6.a are the contours of both z-sides with dz offsets of IP. The corresponding dE/dx beam profiles are plotted in Fig. 1.6.b.

The detector option is favorable radiation tolerant strip detectors to measure electron showers in z-axis. Diamond detectors are favorable for the high carrier mobility, with electron and hole mobilities in the range of 2000–2800 $\mathrm{cm}^2/\mathrm{Vs}$ [6]. The wide bandgap of 5.47 eV [7] minimizes dark noise, while the strong covalent bonds in the diamond lattice provide a carbon atom displacement energy of approximately 43 eV [8], which grants the material superior radiation hardness.

Diamond detectors are employed in beam monitoring in collider experiemnt [9–11]. The radiation hardness has been tested to an neutron dose of 3.3×10^{17} $\mathrm{n(1MeV)/cm}^2$ [12–14]. The results show that single-crystal diamond-based detectors can maintain low-

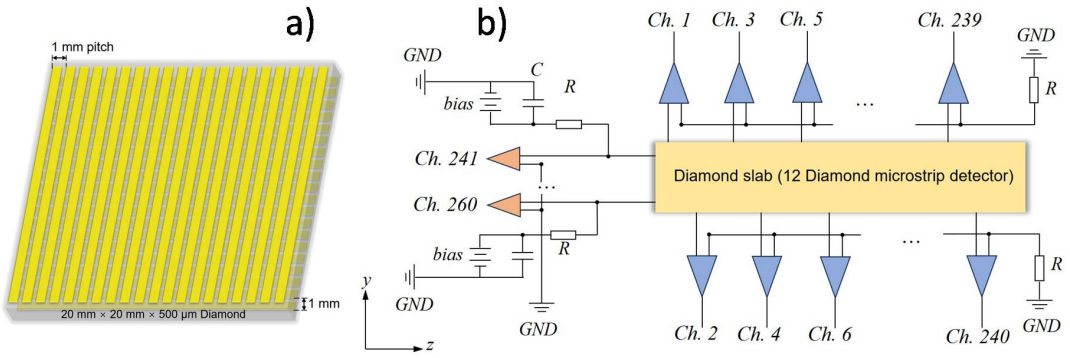

Figure 1.7 a) Schematic of the microstrip diamond sensor with orthogonal front-side and backside microstrips, featuring a 1 mm pitch; b) Illustration of the microstrip readout for a diamond slab, where the front-side microstrips (Channels 1˘240) are connected to preamplifiers for measuring z-axis IP offsets, while the backside microstrips (Channels 241˘260) are connected to high voltage for measuring y-axis IP offsets.

noise operation at equivalent radiation levels exceeding 10 MGy, with signal attenuation corrected through calibration.

The newly developed synthetic diamond technology has significantly reduced defect densities, making low-cost diamonds more readily available for large-scale applications. The electronic-grade diamonds grown by chemical vapor deposition (CVD) are instrumented as strip diamond detectors. The prototype diamond of CVD-grown wafer are fabricated with microstrip electrodes with 1 mm pitch on the front face of a 20×20 mm^2, 500 μm thick crystal. Twenty strips of 0.8×19 mm^2 are implemented with 0.2 mm gaps on the front surface which is illustrated in Fig. 1.7.a. Electrodes on the backside have the same pattern perpendicular to the front.

The electrode implementation requires the diamond surface being oxygen-terminated, which facilitated a reliable Ohmic contact between the metal electrodes and the diamond crystal [15]. The electrode is a multilayer metallic stack made by a sequence of photolithography, magnetron sputtering, and electron beam evaporation processes.

The backside electrodes of a fabricated diamond detector are connected to high voltage. The electric field can be raised to 2 V $/\mu m$, for the ionization charge collection reaching 100% efficiency.

The luminosity monitor slab is propose for an assembly of 12 diamond wafers comprises a total 240 strips, and the readout circuits are illustrated in Fig. 1.7.b. The front-side electrodes (channel 1-240) are configured perpendicular to the beam-pipe direction. The backside with strips parallel to the beam-pipe are interconnected to form a total 20 readout channels (channels 241–260). The shower center of originated electrons will be identified. By balancing the spectra of diamond slabs on both sides of the IP, the $x - y$ positions of electron beams and the IP in z-axis to be tuned and monitored within 1 μRad in angles to the LumiCal.

1.0.3 Beam Position Monitor

The beam steering devices around the IP include the BPMs positioned inside flanges on both z-sides, and on dual pipes before the quadrupole magnets. Illustrated in Fig. 1.8.a is the beam-pipe locations of button-type BPMs. In Fig. 1.8.b to d are the BES II measurement of BPM pulses with single positron beam in 4-pole and dual beams in 8-pole BPMs.

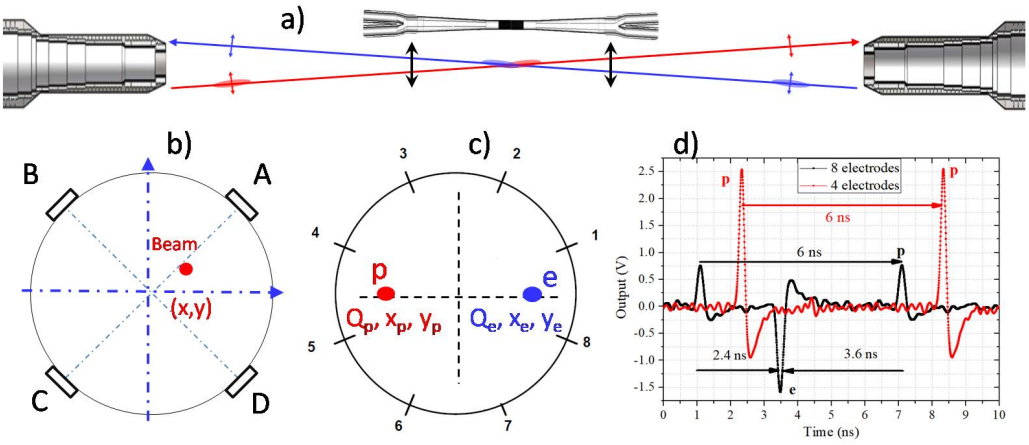

Figure 1.8 The beam position monitors (BPMs) inside flanges will have detect beam bunches that can steer the IP z position. The BPMs single beam pipes before the quadrupole magnets can be precise to 1 μm on the beam x,y positions.

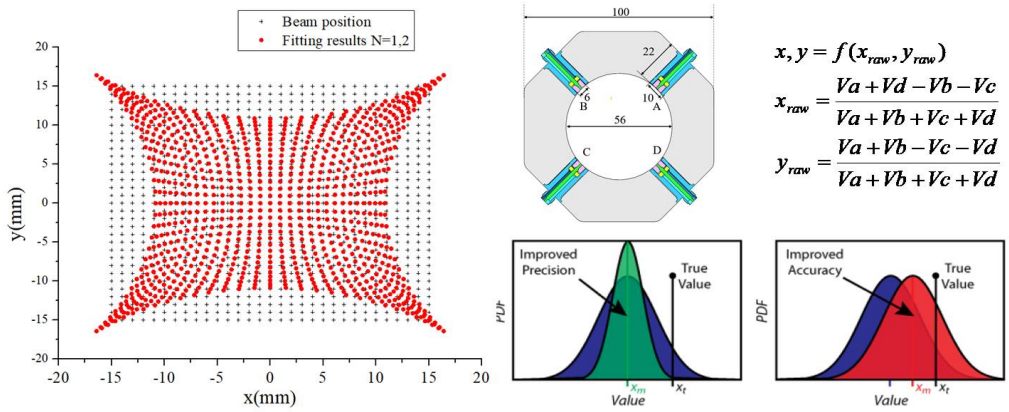

Figure 1.9 The beam position monitors (BPMs) inside flanges will have detect beam bunches that can steer the IP z position. The BPMs single beam pipes before the quadrupole magnets can be precise to 1 μm on the beam x,y positions.

The pulse heights correlates the beam positions, which are calibrated to measure the true x-y position of the beam currents.

In Fig. 1.9 the BPM field and the iteration for the true beam position is shown. The resolution at CEPC is designed for 1 μm, and the accuracy is estimated for $\sim$ 50 μm. The accuracy shall be improved with the survey of the BPM positions.

The Bhabha detection will rely on the BPMs for the IP position at CEPC. By the survey precision on the BPM positions to 1 μm, and by steering the beam with timing precision to 150 ps, the IP position can be precise to 1 μRad, that is required for detecting Bhabha events.

The LumiCal Si-wafers are mounted on the beam-pipe supported by the flanges, while the BPMs are inserted inside the flanges. The LumiCal reference positions shall be the outgoing beam-pipe center at the flanges. The online position deviation is coherent witht the BPMs. In detector assembly, we shall focus on the survey precision on mount the BPMs and the relative Si-wafers positions.

1.0.4 LumiCal acceptance

The LumiCal detector acceptance is optimized for elastic scattering of Bhabha events, with electrons boosted toward outgoing beam pipe direction. A lower θ fiducial angle to the beam center yield larger acceptance. The distribution of scattered electrons is simulated with the BHLUMI. Illustrated in Fig. 1.10.a are the θ distributions of scattered electrons at CMS frame and being boosted for the 33 mRad beam crossing in Lab frame. The back-to-back angles are also plotted in Fig. 1.10.b.

The event selection for the BHLUMI generated Bhabha electrons has applied parameters previously employed in LEP applications. The Acc0 requires $10 < \theta 80$ mRad in CMS

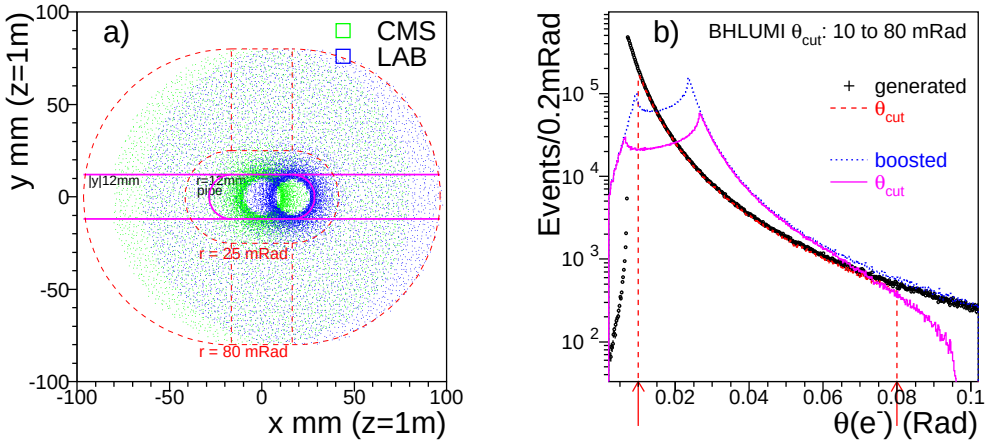

Figure 1.10 a) scattered electron distributions of BHLUMI simulations at CMS frame and after boost for the 33 mRad beam crossing at CEPC. Events are generated for $10 < \theta < 80$ mRad. The Acc0, Acc1 are selections according to the BHLUMI for LEP applications. b) the back-to-back angles of e^+ and e^- are plotted for the generated and boosted, and the Acc0 selected with and without radiative photon.

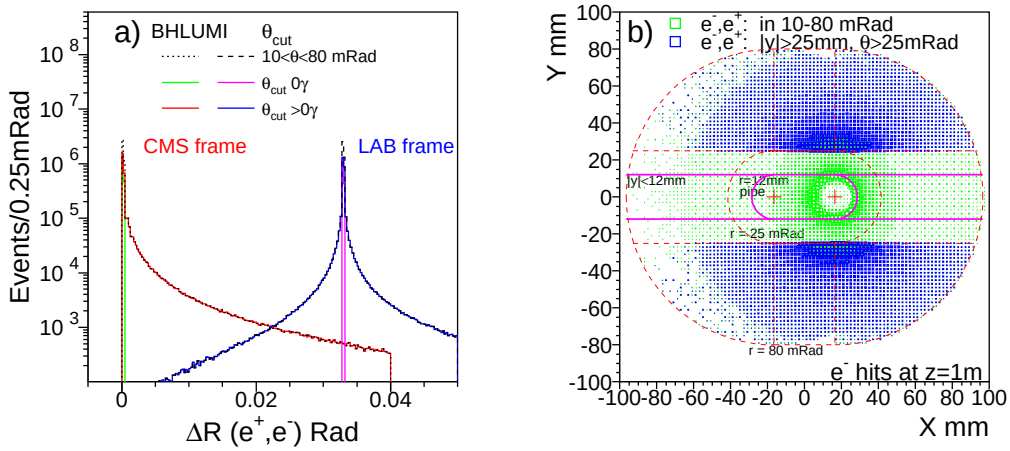

Figure 1.11 a) scattered electron distributions of BHLUMI simulations at CMS frame and after boost for the 33 mRad beam crossing at CEPC. Events are generated for $10 < \theta < 80$ mRad. The Acc0, Acc1 are selections according to the BHLUMI for LEP applications. b) the back-to-back angles of e^+ and e^- are plotted for the generated and boosted, and the Acc0 selected with and without radiative photon.

	CMS generated Th1, Th2 (mRad)	e^-.or. e^+ to pipe centers (mm)	Single e^- in (mm)	(mm)	Both e^-.and. e^+ in (mm)	(mm)
	10 to 80	$10 < r, \|y\| < 80$	$r > 20$	.and. $\|y\| > 20$	$r > 20$	.and. $\|y\| > 20$
σ (nb)	1172.45	1217.45	217.20	137.46	140.74	131.21
	10 to 80	$10 < r, \|y\| < 80$	$r > 25$	.and. $\|y\| > 25$	$r > 25$	.and. $\|y\| > 25$
σ (nb)	1172.45	1217.45	133.42	82.20	85.89	78.08
	10 to 120	$10 < r, \|y\| < 120$	$r > 25$	.and. $\|y\| > 25$	$r > 25$	.and. $\|y\| > 25$
σ (nb)	1181.94	1226.98	144.59	91.34	96.94	87.18

Table 1.1 LumiCal acceptance for Bhabha scattered electrons are simulated with the BHLUMI. Ten million events are generated. The cross section are listed for both e^- and e^+ in the azimuthal angle range (Th1,Th2) in CMS frame, with the center of mass energy to initial $s'/s > 0.5$. The boosted e^- or e^+ in the corresponding LumiCal acceptance of Th1$< r, |y| <$Th2 at $|z| = 1$m ($r =$ radius to near beam-pipe center) are also listed. With a single e^-, and both e^-, e^+ selected for the radius and $|y|$ larger than 20 and 25 mm at $|z| = 1$m are listed. The acceptance cuts on radius and $|y$ are illustrated in Fig.1.11.b.

frame, and the Acc1 for $s'/s > 0.5$ with s' the invariant mass of scattered e^+, e^-. The boosted distributions in Fig. 1.10 are selected for the detector acceptance with $r > 25$ mm to the beam centers at $|z| = 1000$ mm, corresponding to $\theta > 25$ mRad, and $|y| > 25mm$ with a flat edges parallel to the race-track beam-pipe surfaces.

In Fig. 1.11 are the distributions of event selections a) with one electron in fiducial region, and b) both electrons in fiducial region. The cross sections are derived for the BHLUMI calculation and the acceptance in fiducial region, which are listed in Table 1.1, the cross sections of generated to the selected, with one or both electrons detected are listed, for the lower θ cuts of 20 and 25 mRad. The slight lower angle has the near twice the cross section. The boost effect push events along the x-axis into the beam-pipe, thus gain is only about 10% asking for both electrons detected. For easier instrumentation, that is reason to cut off band corresponding to $|y| < 25$ mm at $|z| = 1000$ mm.

1.0.5 Detecting radiative Bhabha events

The BHLUMI generator offers the most precision of 0.037% precision [2] with uncertainties of missing photonic $\mathcal{O}(\alpha^2 L)$ and the hadronic $\Delta\alpha_{had}$ corrections. New calculations with complete NNLO may reach 10^{-1} precision. Radiation Bhabha events cause deviation of electron directions that may smear the event counting crossing the θ_{min} fiducial edge. Therefore measurement of $e^+e^-\gamma$ with ISR and FSR photons are critical to testify the systematic due to radiative Bhabha effect.

Illustrated in Fig. 1.12 are the comparison of BHLUMI and the newly reported ReneSance program. In a) the Bhabha cross section with $\theta_{min} > 30$ mRad is plotted for the CEPC center-of-mass energies. The NLO radiation photon momentum are compared in b). The photon energy spectra of both programs agree well.

The photons of BHLUMI are simulated with the YFS exponentiation, for the interaction of $e^+e^- \to e^+e^-(n\gamma)$. Photons are not indicated for its radiative source electrons. Illustrated in Fig. 1.13.a are energies of the scattered electron versus the most energetic photon in the same hemisphere. The most energetic photon in a event is analyzed for the opening angles to the electrons, and are identified for the mother electron to be an initial

(ISR) or final state radiation photon (FSR), in the LumiCal front LYSO acceptance of $|y| > 12$ mm at $|z| = 647$ mm. In Fig. 1.13.a photon energy versus the opening angle to the closest electron, thus identified as ISR or FSR. ISR photons shall have a large angle to enter the Si-wafer, and the angle to the scattered electron are not correlated by a large angle of > 15 mRad. The FSR photon accompany its mother electron with the opening angle mostly below 5 mRad (91%).

The BHLUMI simulation has 10 M events generated in the θ range of (Th1,Th2) of (10,80) mRad. The e^+ and e^- traveling in each z-direction have 39.7% of them accompanied with radiative one or more photons with energies > 5 MeV. The most energetic photon is identified to be an ISR (20.4%) or a FSR (19.4%). In Table 1.2 the events with both scattered e^+ and e^- accepted in front of the LYSO ($|z| = 647$ mm) with $|y| > 12$ mm are counted for the fractions with photon, with > 0.1 GeV photon, wand with photon $|y| > 12$ mm in the LYSO acceptance.

The ISR to be detected in LYSO has a minimal 18.5 mRad (atan(12/647) off the colliding electron, therefore the event fraction is small (0.89%). The scattered electrons closely accompanied with a FSR is plenty (13.8%). To distinguish the FSR with an opening angle of 5 mRad (8.9% of 0.1 GeV FSR), from the electron, the event fraction is 2.96%.

The e, γ separation is conducted with the hits on Si-wafer and LYSO bar dE/dx deposits. The LYSO segmentation of 3×3 mm^2 corresponds to a pitch of 5 mRad. Plotted in Fig. 1.14.a are the radius of scattered electron in the LAB frame, versus the opening angle to the photon in same z-hemisphere. FSR photons are closely accompanied, and ISRs are in to bands with e, γ in the same y sides or opposite. The electron hit positions with an ISR or FSR are plotted in Fig. 1.14.b. With an ISR the electron hits are scattered more toward larger radius.

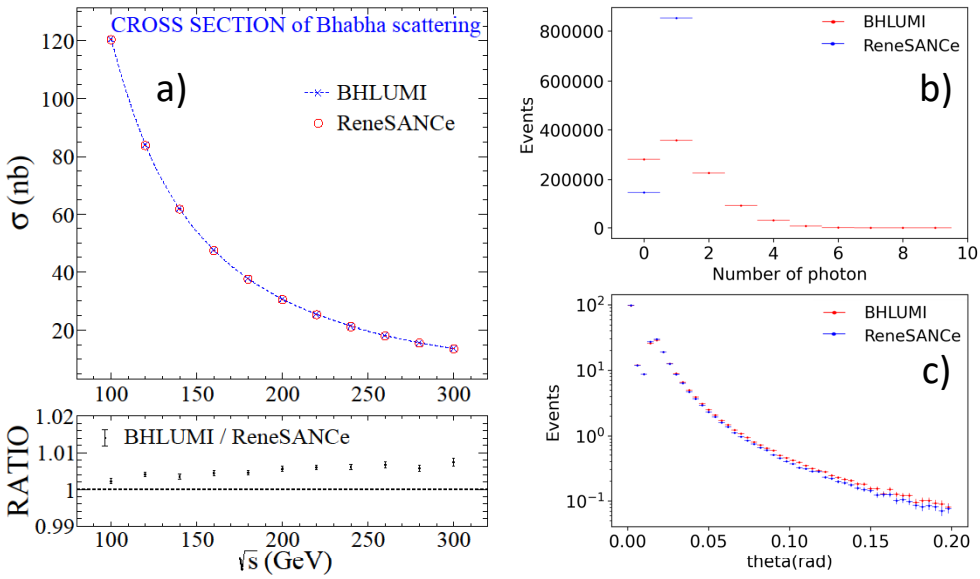

Figure 1.12 Bhabha events are simulated with the BHLUMI and ReneSANCe programs which agree well on cross section. The cross sections of BHLUMI and ReneSANCe is plotted in a) as functions of $\sqrt{s}$. The ratio of them deviating around 0.5% are also plotted. The BHLUMI of YFS exponentiation produces n photons shown in b). The ReneSANCe calcuates NLO diagrams to produce one radiative photon. The opening angles of photons to electrons are applying same mechanism, and show good agreement in c).

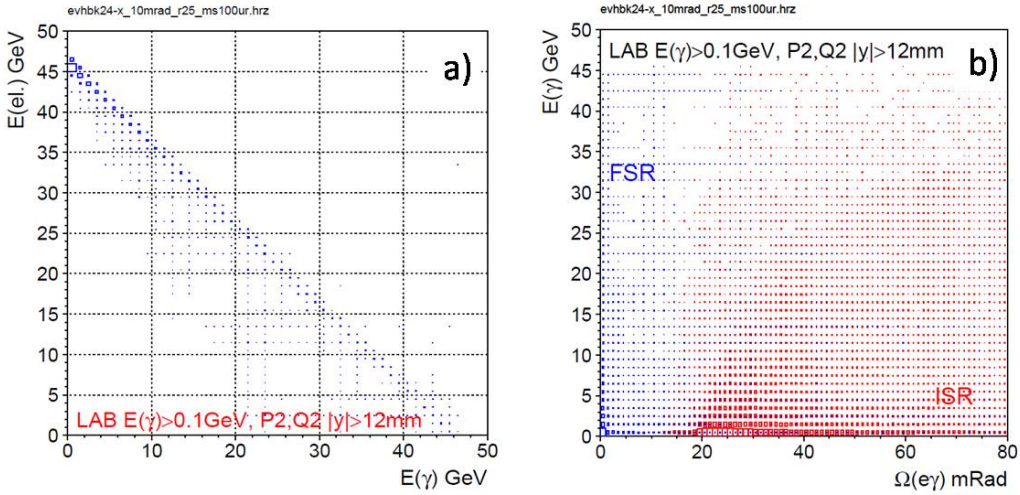

Figure 1.13 The most energetic photon is identified as an ISR or FSR by the opening angle to the closest electron: a) energies of the scattered electron versus the most energetic photon in the same hemisphere; b) photon energy versus opening angle of the most energetic photon to the scattered electron in the same hemisphere.

	$\|y(e^+)\|, \|y(e^-)\|$ > 12 mm		$\|y(e^+)\|, \|y(e^-)\| > 12$ mm; $E_\gamma > 0.1$ GeV			$\|y(e^+)\|, \|y(e^-)\|, \|y(\gamma)\| > 12$ mm; $E_\gamma > 0.1$ GeV			
	$e^\pm, 0\gamma, n\gamma$	$e^\pm$,$n\gamma$	$e^\pm$,$n\gamma$	$e^\pm$,ISR	$e^\pm$,FSR	$e^\pm$,$n\gamma$	$e^\pm$,ISR	$e^\pm$,FSR	$\Omega(e$,FSR) > 5 mRad
events	1405230	631622	445566	233828	211738	206845	12440	194405	41612
ratio	100%	44.9%	31.7%	16.6%	15.1%	14.7%	0.89%	13.8%	2.96%

Table 1.2 Bhabha events of BHLUMI generated in (Th1,Th2) of (10,80) mRad are boosted to the LumiCal acceptance of $|y| > 12$ mm. The events ratio with $E(\gamma) > 0.1$ GeV, and the most energetic photon being an ISR or FSE are selected by the smaller opening angle to electrons. The selections are listed for θ to beam centers and y cuts in front of LYSO at $|z| = 647$ mm, corresponding to the lowest LAB frame of 18.5 mRad.

1.0.6 LumiCal detector simulation

The LumiCal design has to incorporate the space available in the MDI region, to enlarge the θ coverage. Illustrated in Fig. 1.15 is the drawing of LumiCal modules mounted on the race-track pipe. The Si-wafers measuring electron impact position are located closer to the beam-pipe for the lowest θ coverage with the minimum upstream beam-pipe materials. Si-wafer with strips in pitches of, e.g. 50 μm, can reach better than 5 μm resolution.

Although the Si-wafer can be instrumented to reach 5μm, the low angle causes a large beam-pipe traversing thickness. With a 1 mm thick Be beam-pipe, the traversing distance at 0.02 mRad is (1/sin(0.02)) 50 mm, corresponding to $0.14X_0$. With Al, 1 mm thick, it is $0.56X_0$.

To minimize multiple scattering effect, the beam-pipe is proposed for inserting flat Be low-mass windows between $|x| < 6$ mm. The half-round pipe on the sides are double-layer Al pipe containing cooling water circulating from flanges toward IP. The temperature variation of the beam-pipe is also shown in Fig. 1.15. The simulation of multiple scattering using 50 GeV muon is illustrated in Fig. 1.16.b before the frange, and Fig. 1.16.c after

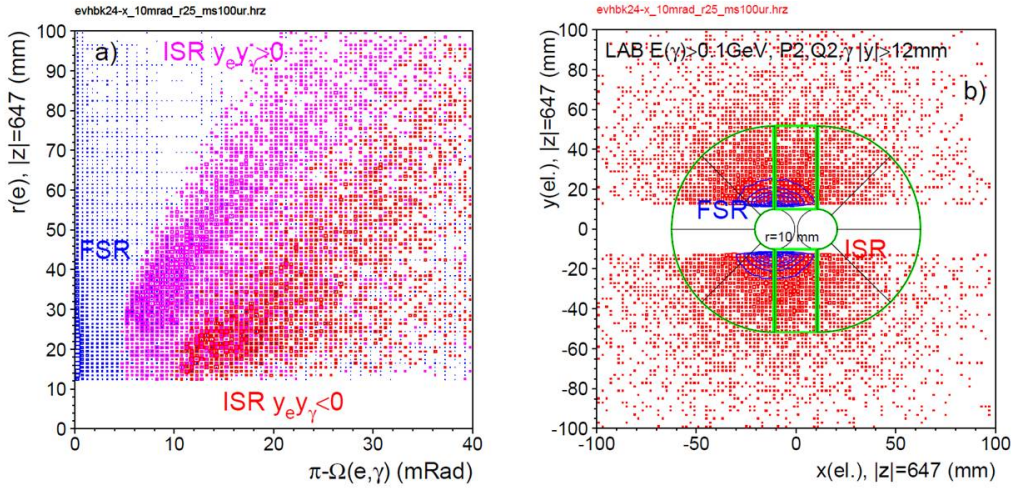

Figure 1.14 Event with radiative photon ($E_\gamma > 0.1$ GeV) are plotted for e, γ separation. a) the scattered electron position in front of LYSO is plotted for the LAB frame x-y radius vs e, γ opening angle in the same z-hemisphere. b) the electron hit positions in LAB x-y frame are shown. In case of FSR both e and γ are close beam pipe; with an ISR, e and γ are spread wider.

passing $2X_0$ of LYSO, $4.3X_0$ of steel flange (30 mm) and bellow (45 mm) on to the 200 mm long LYSO bars.

The detector option for LumiCal is constrainted by the space and weight. The $2X_0$ LYSO crystal covering the radius of 42 mm, 23 mm in length, has a total weight of 0.45 kg ($\pi \times 4.2^2/2 \times 2.3$, density 7.1 g/cm^3, Fig. 1.15). the long LYSO has 10 layers of $10 \times 10 \times 200$ mm^3 bars, corresponding to a total weight of 22.3 kg ($\pi \times 10^2/2 \times 20 \times 7.1$).

The distribution of Bhabha electrons and radiative photons are generated with the BHLUMI. The detector simulation with GEANT provides multiple scattering and electromagnetic showers in LumiCal. Bhabha electrons are distributed near the outgoing pipe. The smearing due to multiple scattering with BHLUMI generated electrons are plotted in Fig. 1.17.a for the hits on the front Si-wafer at $|z| = 560$ mm.

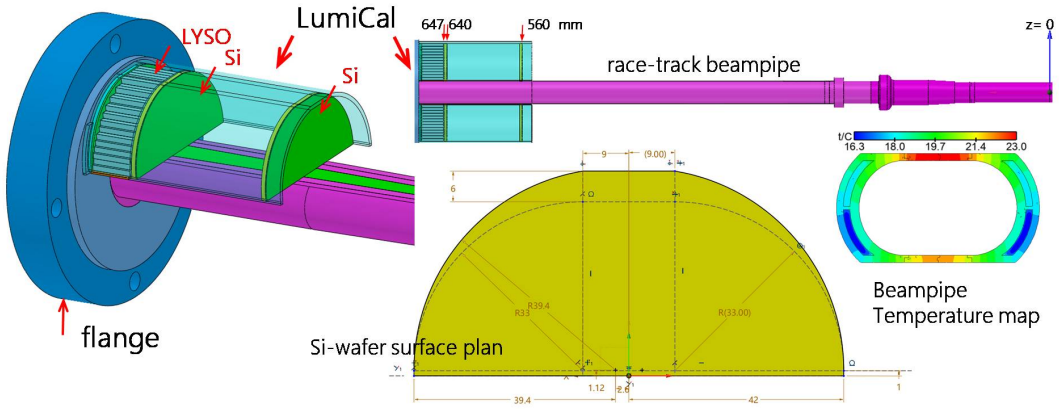

Figure 1.15 Mechanical drawings of the LumiCal modules before the flange of race-track beam-pipe. The two Si-wafers and $2X_0$ LYSO crystal bars are contained in half circular tubes above and below the pipe. The cooling of beam pipe has the water injected from the flange toward IP within the double Aluminum layers on the sides with the temperature map illustrated.

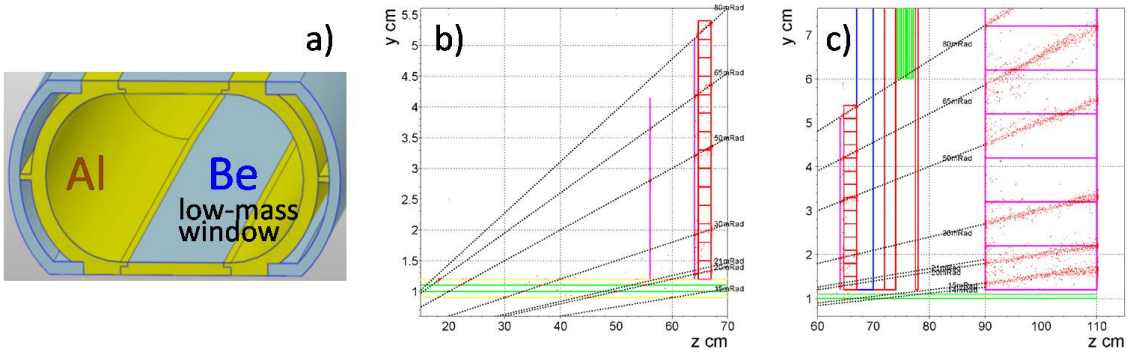

Figure 1.16 a) the beam-pipe has low-mass window with 1 mm thick Be flat layer of 6 mm wide. The multiple scattering is simulated with GEANT The hits of 50 GeV muons are simulated at fixed theta angle traversing Si-wafers and LYSO before flange, and c) passing through flange, bellow to the $17.4X_0$ LYSO.,

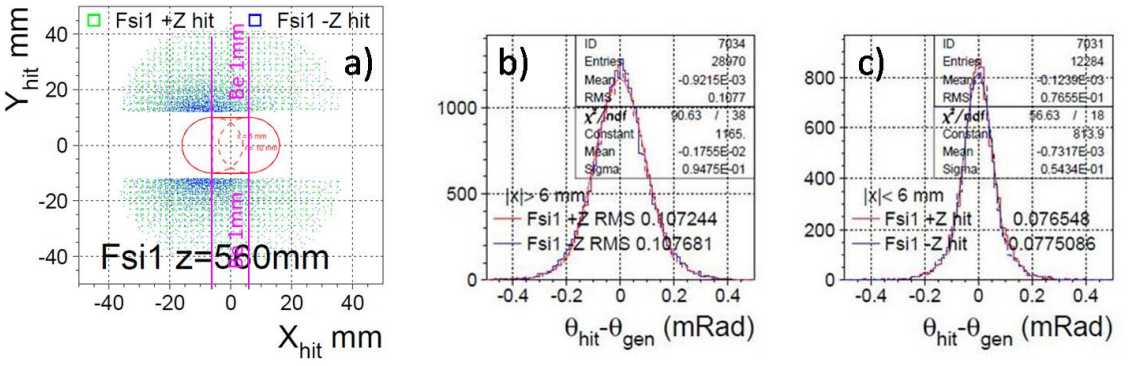

Figure 1.17 BHLUMI generator electrons at $\sqrt{s} = 92.3$ GeV are injected in GEANT LumiCal simulations for multiple scattering effects. a) the hits of electrons on the front Si-wafer at $|z| = 560$ mm. The beam-pipe has 6 mm wide Be low-mass window as indicated, surrounded by 1 mm Al round pipe. The hits to the generated projection is plotted in b) and c) for $|x|$ outside/within 6 mm, respectively, with Gaussian fits.

The smearing due to multiple scattering on the Bhabha electron hits, to the projection of generated, are plotted in b) and c) for the hits outside/inside the $|x| < 6$ mm Be window. The Gaussian fits yield

$$|x| > 6 \text{ mm}: \quad m = -1.8 \pm 0.6\ \mu\text{Rad} \quad 95 \pm 0.6\ \mu\text{Rad} \tag{1.3}$$

$$|x| < 6 \text{ mm}: \quad m = -0.7 \pm 0.6\ \mu\text{Rad} \quad 54 \pm 0.7\ \mu\text{Rad}. \tag{1.4}$$

The effects smearing by multiple scattering are symmetric for both the x-range within the Be low-mass and outside in the Al pipes. The errors on the mean are less than 1 μRad. At $|z| = 560$ mm, most electrons enter Si-wafer of $|y| > 12$ mm have the $\theta > 21$ mRad, corresponding to $\Delta\theta = 1$ μRad for $\Delta\mathcal{L}/\mathcal{L} = 10^{-4}$ (eq. 1.2).

The smearing by multiple scattering will require test-beam studies to confirm the widths. The simulation with 1 mm Be and Al thick pipe, the width is a factor two, although the Al radiation length is four times thicker. The simulation in Fig. 1.17 has applied the beam spot size of $\sigma_x = 6$ μm and $\sigma_z = 9$ mm ($\sigma_y = 35$ nm is neglected). The beam-cross results to an overlap of $\sigma_z = 380$ μm in z. If σ_x, σ_z are 0, the Gaussian widths reduce by about 5%. For the accuracy on event counting at fiducial edge, the smearing effect shall be measure so as to measure the mean and error. The two Si-wafer will cross refer each

other, to measure the multiple scattering spectra, so as to determine the error and the mean on the Bhabha selection fiducial edge.

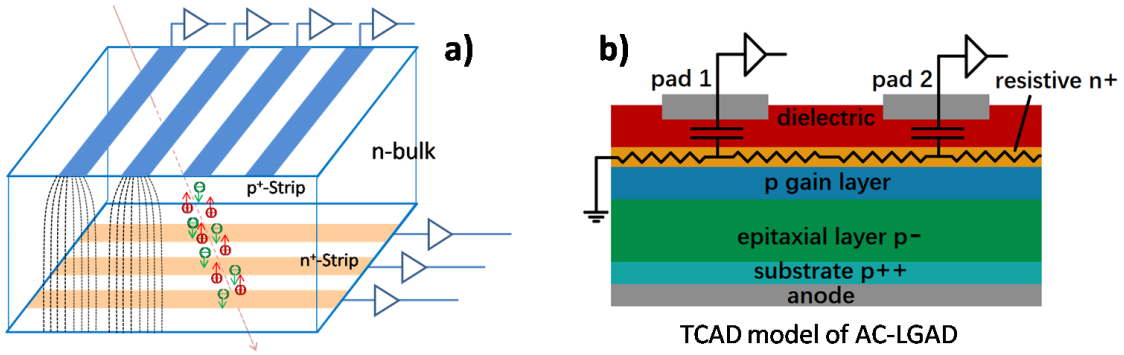

Figure 1.18 Si-detector options are shown for a) conventional double-sided detector with strips implemneted on both side of the wafer; AC-LGAD detector with AC-coupling layers on top of the LGAD pads. The douple AC layers is proposed for 2D readout of the electron hits.

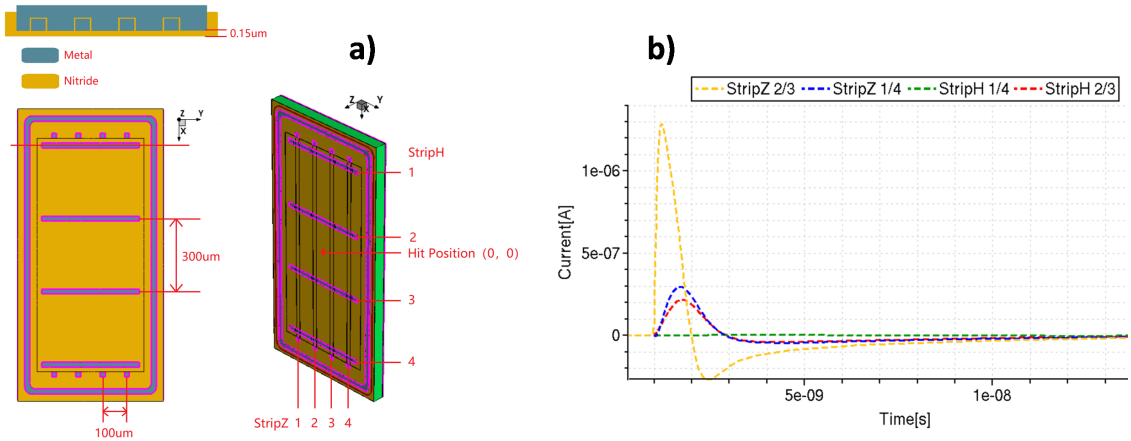

Figure 1.19 A TCAD simulation of 2D AC-couplng LGAd design is shown in a) with the AC coupling strips in 100 μm pitch and the length of 300 μm. The read-out metal are inslulated in two directions for 2D redout. The charge collected are showing in b) for the electron impact at center strip. The charge are plotted for center (orange), adjacent strips (blue/red, edge contacted) and corner (green) strip.

The Si-detectors are chosen for low mass and resolution of electron impact positions. The options include 2-dimensional (2D) Si-strip detectors shown in F and the newly developed AC coupled Low Gain Avalanche Detector (AC-LGAD) shown in Fig. 1.18.b. The AC-LGAD is an option for the Si-Tracking detector of CEPC. We propose for a new dual AC doupling layers for 2D readout, with the front-end and readout following the Si-Tracker program.

The T-CAD simulation of the 2D AC-LGAD is shown in Fig. 1.19.a. It is study structure containling long AC coupling strips in 100 μm pitch with the length of 300 μm. The charge collections are shown in Fig. 1.19.b for the strips around a electron impact position. The charge of direct hit strip (orange dashed) show a current much higher than those of direct adjacent (blue, red-dashed), and the conered strips (green-dashed) show a flat charge collection.

1.0.7 LYSO calorimeter simulation

The low-mass of beam-pipe suppresses electro-magnetic shower secondaries to occur before the Si-wafer. Behind the second Si-wafer are $2X_0$, 23 mm long LYSO arrays before the flange (Fl.LYSO, that is finely segmented in 3×3 mm^2, to detect Bhabha electron hits and for e/γ separation to identify radiative photon. The long LYSO array of $17.4X_0$, 200 mm long, before the Quadrupole magnet (QM.LYSO) measure the beam electron with energy deposition if shower secondaries traversing LYSO ($2X_0$), flange (30 mm Fe) and bellow (45 mm Fe). The accumulated upstream materials account for $6.3X_0$.

The length of QM.LYSO maybe reduce by the quadrupole position. The electron shower detection is compared for the QM.LYSO lengths of 150 and 210 mm, shown in Fig. 1.20, with the front positions at $|z| = 830mm$. The front material accounrted for the FL.LYSO of $2X_0$ and the flange, bellow of $4.3X_0$. The 50 and 120 GeV shower profile (Fig. 1.20.a) contains the shower-maxima. The sum of dE/dx ((Fig. 1.20.b) of both crystal lengths are 2.5 GeV and 4.3 GeV for 50 and 120 GeV electrons. The energy deposits

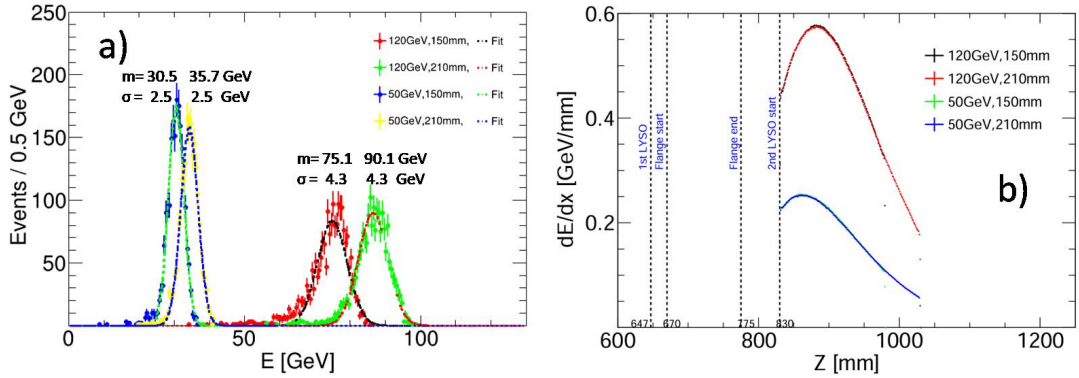

Figure 1.20 The long LYSO bars behind bellow are simulated for the lengths of 150 mm or 210 mm. The energy deposits in z-axis are plotted in a). The energy resolutions of the sum dE/dx are plotted in b) with Gaussion fits. The means differ with cyrstal lengths, the Gaussian σ are compatable, to be 2.5 GeV (4.3 GeV) for 50 GeV (120 GeV) electrons, respectively.

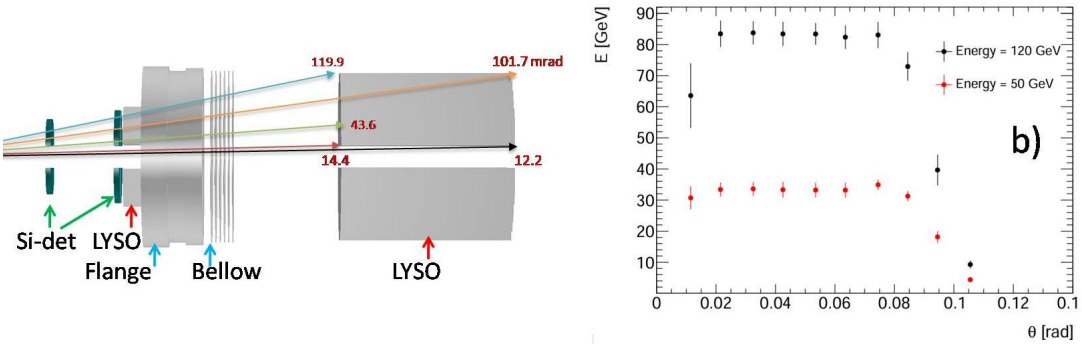

Figure 1.21 The long LYSO detector acceptance versus the electron theta is scanned along ver vertial y-axis, witht the angles illustrated in a). The sum dE/dx distributions are plotted in b) for the electron energies of 50 GeV and 120 GeV. The materials in frant include 2 X_0 short LYSo and $4.4X_0$ flange and bellow, that takes away about 40 (30) % of the shower dE/dx for 50 (120) GeV electrons, respectively. The uniform acceptance distributed from 20 to 75 mRad.

with 150 and 210 mm crystals differ for the fractions of 62% and 71%, respectively. For identification of beam electrons, the shorted crystal with lower sums of dE/dx has quality similar to the long crystal.

The acceptance of angular dependence is illustrated in Fig. 1.21, with the electrons shooting across the QM.LYSO along the y-axis. The sums of dE/dx in the long LYSO are plotted in Fig. 1.21.b. The uniform plateau covers from 20 to 75 mRad for the LYSO front surface of $|y| = 10$ mm to 100 mm.

The GEANT simulation of electromagnetic shower profiles and dE/dx depositions are plotted in Fig. 1.22 for a 50 GeV electrons at a fixed direction of $\theta = 32$ mRad vertically at y-axis, that is centered at a LYSO cell. The shower profiles of secondary particles on

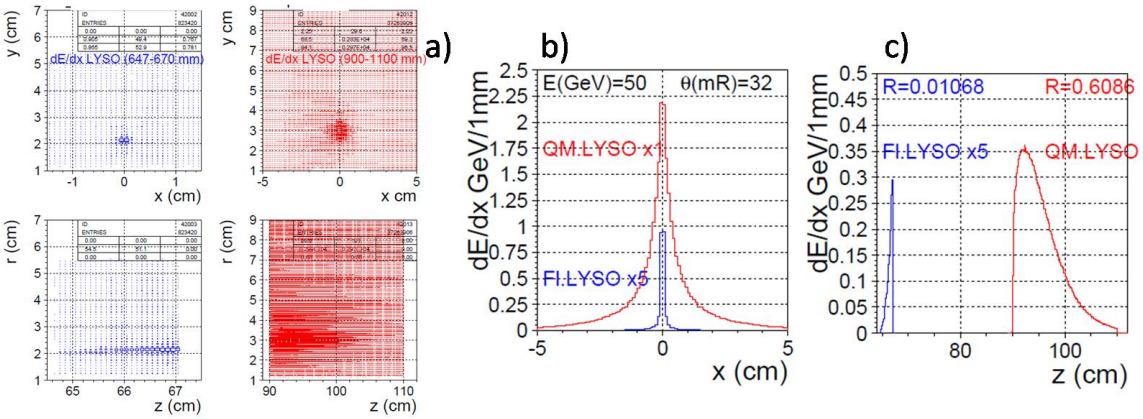

Figure 1.22 Electromagnetic shower of 50 GeV electrons at 32 mRad vertical at 90°. The dE/dx deposits are plotted in the LYSO modules of $2X_0$ before flange (Fl.LYSO) and $17.4X_0$ before the quadruple magnet (QM.LYSO). In a) the dE/dx deposits are plotted in x-y and r-z positions with $r = \sqrt{(x^2 + y^2)}$ the radius in LAB frame , projection in x axis and z axes, that is normalized per event.

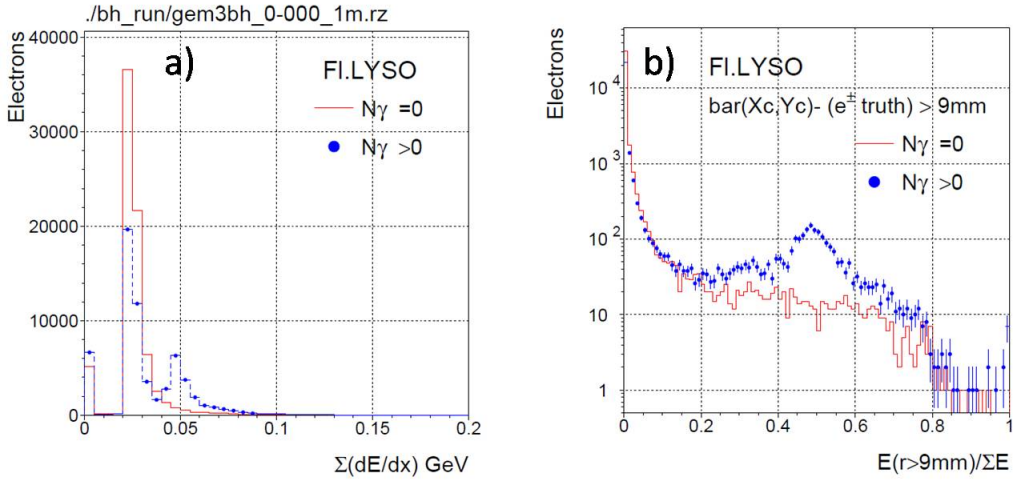

Figure 1.23 The scattered electrons of BHLUMI with projected truth directions entering LYSO at $|z| = 64.7$ mm, $|y| > 12$ mm, are simulated with GEANT. The energy deposits of electrons in a half-circle module are plotted in a). The double peak with photon could be with an FSR adjacent to the electrons. The fraction of energies in LYSO bars 9 mm off the projected electron direction is plotted in b), indicating the observable of a photon that can be identified by the LYSO bar segmentation.

the front and back LYSO arrays are plotted for dE/dx profiles in x-y and r-z distributions in a). The dE/dx projections in x and z axes are plotted in b) and c). The shower deposits in Fl.LYSO are narrowly distributed in the 3 mm segmentation width. The shower profiles in the long 10×10 mm^2 are also well contained in a LYSO bar. The front $2X_0$ shower deposition is rather small, accounted for only 1 % of the 50 GeV electron energy. The deposition in QM.LYSO after $6.3X_0$ accounts 61 % of the electron energy.

The e/γ identification for radiative Bhabha events is conducted with the BHLUMI generated electrons and photons boosted for the 33 mRad beam crossing, to the LumiCal GEANT simulation. The photons could be ISR or FSR. The scattered electrons entering the $2X_0$ LYSO arrays, of $|y| > 12$ mm are searched for energy deposition in LYSO bars in 3×3 mm^2 segmentation. In Fig. 1.23.a, the energy deposits are compared for Bhabha with and without incident photons which could be ISR or FSR. On a module of LYSO bars in the same y, z hemisphere, electrons accompanied with an FSR show in the twice dE/dx location. The distribution of about 1/4 in double peak corresponds to the FSR accompanies with a scattered electrons in a Bhabha event that has a ISR or FSR photon.

The separation of FSR to the electron is demonstrated in Fig. 1.23.b for the energy deposited in cells of center 9 mm away from the electron projected position. The enhanced peak indicate the presence of a photon hit.

1.0.8 Systematics on integral luminosity

The measurement of luminosity at CEPC is the counts of Bhabha events $N_{\rm Bh}$ with both scattered electrons detected in coincidence in LumiCal modules on both z-sides. The luminosity is derived by $\mathcal{L} = N_{acc}/\epsilon\sigma^{vis}$ 1.2, where ϵ has the systematics on instrumentation and σ^{vis} is the theoretical calculation depending on the precision on fiducial acceptance, that depends mostly on the lower θ edges, to better than 1μRad for 10^{-4} precision as is discussed in Sec. 1.0.1. The tolerance on radius at $|z| = 560$ mm is 0.56μm. The systematic uncertainties on the scattered electron θ can be classified into three categories:

a. Accelerator beam energy precision and spread

At the Z-pole, the beam energy is 45.5 GeV with a spread of 0.13%. The systematics due to beam energy offset causes deviation on the Bhabha cross section. It is estimated with the BHLUMI and reneSANce programs. For the 1×10^{-4} precsion, the beam energy offset shall be smaller than ± 20? MeV.

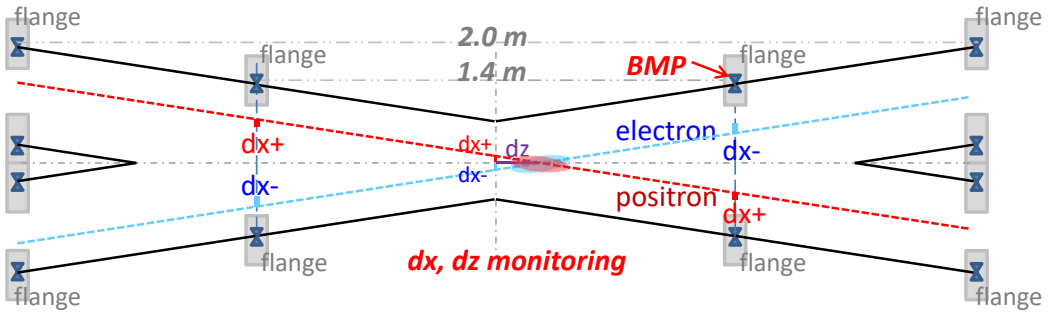

Figure 1.24 The beam currents at IP region is illustrated for offsets to be measured with Beam Position Monitor.

Bhabha cross section is higher with lower center-of-mass energy. The beam energy spread of 0.13% is simulated with a Gaussian distribution for the cross section is weighted accordingly for the $\sqrt{s}$ dependence. For the mean of $E_b = 45.5$ GeV, the correction factor for energy spread is 1.01?

b. Systematics on the beam crossing IP position

The beam collision IP is best measured by the BPMs, measuring beam currents inside the vaccumn pipe. The closest sets are at $|z| = 700$ mm, inside the flanges observing both the electron and positron beams, illustrated in Fig. 1.24. The single beam BPMs in front of the Quadrupole magnet ($|z| = 9800, 1000$ mm) can provide pulses of bunches with respect to the x-y position of the beams.

The bunch sise has the widths of $\sigma_x = 6$ μm, and $\sigma_z = 9$ mm. The 33 mRad bunch crossing reduces z-width to $\sigma_z = 380$ μm. The beam tuning will iterate on the timing of bunches arriving at IP, and the x-y sweeping.

At $\theta = 25$ mRad, the 1μRad offset corresponds 40 μm at $z = 1000$ mm, where the BPM timing precision is required for 1.3 ps. The spacing x-y precision of BPM is better than 1 μm. By sweeping beam currents in x, the crossing point is $z = 0$, and by timing to the brightest luminosity, shall yield the IP to the ideal beam-pipe center.

c. Systematics on measuring electron hits

The scattered electron hits on the LumiCal Si-wafer, with the wafer edges surveyed to better than 1μm.

The effect of multiple scattering to the Bhabha cross section, due to beam-pipe material, is simulated with the BHLUMI distribution of electrons. Assuming the LumiCal has the lower θ edge set for $|y| > 20mm$ at $|z| = 1$ m, corresponding to a varying θ_{min} of the lowest 20 mRad. The multiple scattering is simulated for 100 μRad convoluted on the scattered electron θ and ϕ. Illustrated in Fig. 1.25.a are the electrons hits at LumiCal y edge, with the cut on generated electrons. The multiple scattering deviates electrons in and out of the edge. The two Bhabha elestrons are back-to-back

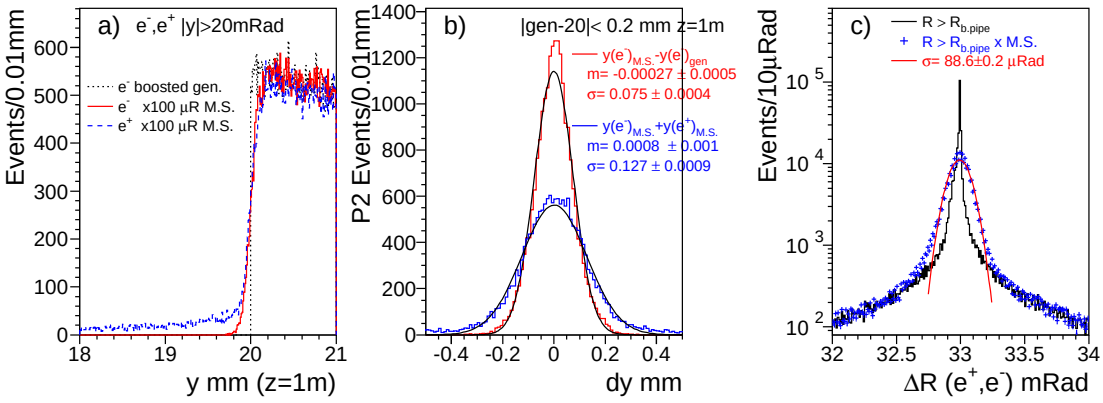

Figure 1.25 The scattered electrons (P2) and positrons (Q2) both accepted within the fiducial edges of LumiCal at $|z| = 1$ m are plotted in a) for the distribuion in $|y|$. The dotted is the BHLUMI generated P2 being cut at $|y| > 20$ mm. The multiple scattering (M.S.) smeared P2 is plotted in red solid line. The Q2 in the other z-side is plotted in blue dashed, where the tail are events having radiative photons. The smearing width is with

symmetric to the out-going beam center, with (x, y) coordinates of $(16.5\ mm, 0)$ at $|z| = 1$ m. the $-y$ distribution of electrons on the other z-side is also plotted to show the electrons of radiative events with large $|y|$ off the cut (blue-line).

The back-to-back tracking of the pair of Bhabha electrons will also provide calibration for detector position. The front silicon layer of the luminosity detector will measure electron impact positions to a few micron. This wafer shall be an 2D fine-pitch strip detector, the position is measured by strips collecting the ionization charges generated by a traversing electron.

d. Systematics on MDI beam-pipe, LumiCal survey and monitoring

The alignment precision of the front-layer Silicon detector is the most critical issue to reach 1 μm in radiaus for the luminosity measurement of 10^{-4}. An online survey system is required to monitor the fiducial edge position for the error on mean of better than 1 μm

The mean of fiducial edge and the systematics uncertainties are the LumiCal design goal.

1.0.9 Summary

The instrumentation of a Luminometer is investigated for detection of small angle Bhabha interaction in the MDI geometry of a reference detector at CEPC. The Luminosity measurement for the CEPC Z-pole statistics is expected for 1? billion events. For the Standard Model measurement, the Luminosity precision is required for better than 10^{-4}.

Bhabha events are elastic scattering of electrons with a large fraction of events accompanied with initial and/or final state photons. The QED calculation of NLO is better than 0.5/with generators of YFS approach or Feynman diagram? approaches. The BHLUMI program is used for all LEP measurements, and will be an reference package for Bhabha simulation.

The challenge on luminosity falls on the precision of fiducial edges for Bhabha event counting with electrons measured relative to the IP. The precision corresponding to a low-theta edge of 20 mRad is 1 μRad, for survey and monitoring of the LumiCal position.

In this Technical Design Report, we have incorporated the race-tack beam-pipe with a inner diameter of 20 mm for the 33 mRad beam-crossing at IP. The precision of LumiCal acceptance is required for the front Si-detector inside the inner beam-pipe flanges. The coordinate reference is the out-going beam pipe center at the flanges with the outer surface position at $|z| = 700$ mm. This is the position the external vacuum lock-up rings in front of the bellow attaches to the flanges. The LumiCal can be surveyed to sub-micron precision measuring the Si-detector and LYSO crystal positions. The external monitoring includes the z positions of flanges relative to the IP, which with the mean of better than 50μm.

The position monitoring includes the BPM system for beam currents and IP with the single measurement of better than 1μm and the mean of sub-micron. We propose for installing Diamond fast monitoring detectors on the sides of beam-pipe between the long LYSO crystals before the Quadrupole magnets. The electron showers of small angle Bhabha traversing the 3 mm thick Cu pipe can be measured for the wide spread of showers in 200 mm, with the centers corresponding to the electron theta angles. The Diamond monitor can provide instant beam electron signals and potentially the online luminosity measurement.

In the simulation for beam spot and multiple scattering, we have investigated the smearing of electrons impact positions is around 50μRad with a 1 mm thick Be low-mass window. The error on mean is smaller than 1μRad. The Bhabha detection precision is concerned on the electron identification including the radiative photon that deviates the electron direction.

The segmentation of the LYSO bars of $2X_0$ inside the flanges calorimeter is considered for the back-to-back detection a pair of Bhabha electrons, and in addition, for e/γ identification of FSR photon. The LumiCal shall be able to measure radiative Bhabha events so as to compare the measurement with the QED calculations.

References

[1] S. Jadach, W. Placzek, E. Richter-Was, B. F. L. Ward, and Z. Was, Upgrade of the Monte Carlo program BHLUMI for Bhabha scattering at low angles to version 4.04, Comput. Phys. Commun. **102** (1997) 229–251.

[2] P. Janot and S. Jadach, Improved Bhabha cross section at LEP and the number of light neutrino species, Physics Letters B **803** (2020) 135319. https://www.sciencedirect.com/science/article/pii/S0370269320301234.

[3] R. Sadykov and V. Yermolchyk, Polarized NLO EW e^+e^- cross section calculations with ReneSANCe-v1.0.0, Computer Physics Communications **256** (2020) 107445. https://www.sciencedirect.com/science/article/abs/pii/S0010465520302083.

[4] S. Jadach, E. Richter-Was, B. F. L. Ward, and Z. Was, Monte Carlo program BHLUMI-2.01 for Bhabha scattering at low angles with Yennie-Frautschi-Suu Comput. Phys. Commun. **70** (1992) 305–344.

[5] H. S. D.R Yennie, S.C Frautschi, The infrared divergence phenomena and high-energy processes, Annals of Physics **13** (1961) 379 – 452.

[6] J. Isberg, J. Hammersberg, E. Johansson, T. Wikström, D. J. Twitchen, A. J. Whitehead, S. E. Coe, and G. A. Scarsbrook, High carrier mobility in single-crystal plasma-deposited diamond, Science **297** (2002) no. 5587, 1670–1672.

[7] G. S. Painter, D. E. Ellis, and A. R. Lubinsky, Ab Initio Calculation of the Electronic Structure and Optical Properties of Diamond Using the Discr Phys. Rev. B **4** (1971) 3610–3622. https://link.aps.org/doi/10.1103/PhysRevB.4.3610.

[8] J. Koike, D. M. Parkin, and T. E. Mitchell, Displacement threshold energy for type IIa diamond, Applied Physics Letters **60** (1992) no. 12, 1450–1452. https://doi.org/10.1063/1.107267.

[9] A. J. Edwards, M. Bruinsma, P. Burchat, H. Kagan, R. Kass, D. P. Kirkby, B. A. Petersen, and T. Pulliam, Radiation monitoring with CVD diamonds in BaBar, Nucl. Instrum. Meth. A **552** (2005) 176–182.

[10] A. Gorišek, V. Cindro, I. Dolenc, H. Frais-Kölbl, E. Griesmayer, H. Kagan, S. Korpar, G. Kramberger, I. Mandić, M. Meyer, M. Mikuž, H. Pernegger, S. Smith, W. Trischuk, P. Weilhammer, and M. Zavrtanik, ATLAS diamond Beam Condition Monitor, Nucl. Instrum. Meth. A **572** (2007) no. 1, 67–69. https://www.sciencedirect.com/science/article/pii/S0168900206019838.

[11] A. Kornmayer, The CMS pixel luminosity telescope, Nucl. Instrum. Meth. A **824** (2016) 304–306. https://www.sciencedirect.com/science/article/pii/S0168900215011936.

[12] L. Bäni, A. Alexopoulos, and e. a. Artuso, A study of the radiation tolerance of poly-crystalline and single-crystalline CVD diamond to 800 Me Journal of Physics D: Applied Physics **52** (2019) 465103.

[13] N. Venturi, A. Alexopoulos, M. Artuso, and F. e. a. Bachmair, Results on radiation tolerance of diamond detectors, Nucl. Instrum. Meth. A **924** (2019) 241–244.

[14] Y. Liu, J. Zhang, F. Wu, M. Qi, L. Hei, and F. Lv, The Raman Spectroscopy and XPS investigation of CVD diamond after fast-neutron irradiation, Materials Today Communications **22** (2020) no. May 2019, .

[15] S.-F. Fan, B. Liang, X.-H. Zhang, W.-C. Zhang, B. Wang, T.-B. Li, T. Su, B.-J. Liu, V. Ralchenko, K. Liu, and J.-Q. Zhu, Record Low Contact Resistivity of 10^{-8} Ω cm² Ohmic Contacts on Oxygen-Terminated Intrinsic Dia IEEE Electron Device Letters **45** (2024) 2062–2065.